PAPER

Check for updates

Agri-waste derived electroactive carbon–iron oxide nanocomposite for oxygen reduction reaction: an experimental and theoretical study†

Pallavi B. Jagdale, [a] Sai Rashmi Manippady, *[ab] Rohit Anand, [c] Geunsik Lee, [c] Akshaya Kumar Samal, [a] Ziyauddin Khan [d] and Manav Saxena *[a]

Herein, we have utilized agri-waste and amalgamating low Fe^{3+}, to develop an economic iron oxide–carbon hybrid-based electrocatalyst for oxygen reduction reaction (ORR) with water as a main product following close to $4e^-$ transfer process. The electrocatalytic activity is justified by electrochemical active surface area, synergetic effect, and density functional theory calculations.

1 Introduction

In academia and industry, advanced techniques for sustainable energy storage and conversion have received a lot of attention due to the faster depletion of fossil fuels and accompanying pollution. For cleaner power generation, fuel cells and metal rechargeable air batteries are next-generation devices. However, the cathodic oxygen reduction reaction (ORR) in these devices is sluggish due to an exceptionally strong O=O bond energy of 498 kJ mol^{-1}.[1] To lower the energy barrier, it is necessary to use electrocatalysts for bond activation and cleavage. Pt-based catalysts are used commercially which is roughly one-third of the device costs and are usually susceptible to fuel crossover and suffer from poor stability, thus tremendously limiting the massive applications.[2,3] Consequently, for large-scale applications, it is of the utmost importance to develop highly active, stable, and cost-effective ORR electrocatalysts. Specific surface area, and number of active sites are the important factors which affect ORR activity. Also, ORR activity is determined by the overall activity of the catalyst and the exposed active sites.[4]

The non-precious (Mn, Fe, Co, and Ni-based),[5–8] metal–nitrogen–carbon,[9] hetero-atoms doped carbon materials,[10,11] based electrocatalysts have gained attention due to sufficient active sites, close to $4e^-$ reduction pathway, and long-term durability.[12] Further, lignin-rich biomass-derived carbon has

attracted attention to developing greener, economic biomass-based electrocatalysts due to low-cost, high, and stable electrocatalytic activity.[10,13,14] The cost-effective iron/nitrogen co-doped carbon catalysts show good conductivity with higher catalytic activity.[15] In a recent report, Ahmed *et al.* represented Fe NPs inside metal–organic frameworks showing good ORR performance and highly stable catalyst.[16] J. Ren *et al.* synthesized zeolitic-imidazolate-framework-derived Fe–NC catalysts with good ORR activity.[4] Among biomass, bagasse is one of the vital agri-waste due to easy availability, cheap, cellulose, hemicellulose, and lignin-rich.[17,18] To reach out the demands of ORR electrocatalysts by tapping into the potential of biomass-derived precursors, mainly bagasse. We target to synthesise ORR catalysis by using biomass-derived precursors and a simple innovative synthesis technique. In addition to experimentation and electrochemical analysis, we also discussed the theoretical aspects using density functional theory (DFT) calculations to understand the mechanistic part.

Herein, we report an economical carbon–iron oxide composite material using bagasse as a carbon source with optimized Fe^{3+} concentration ions *via* the carbonization process without any additional activation step. The only chemical used in our synthesis is Fe^{3+} precursor, which is significantly cheap, abundant, and non-toxic. We have rationally designed the composite to use the coordinating ability of oxygen groups of cellulose, sugar, and lignin moieties with Fe^{3+} ions. The interaction of Fe^{3+} ions with oxygen functional groups results homogeneously dispersed iron oxide nanoparticles in the carbon matrix upon carbonization at 900 °C (10 °C min^{-1}) in N_2 gas flow. We have synthesized nanocomposites by varying Fe percentage, which is termed as CFe-0 (control), CFe-1, CFe-2, and CFe-3 (carbon–iron oxide nanoparticles composites) and electrochemical studies had been performed to check their ORR activity.

[a] Centre for Nano and Material Sciences, Jain (Deemed-to-be University), Bengaluru, Karnataka-562112, India. E-mail: sairashmi1994@gmail.com; s.manav@jainuniversity.ac.in; manavsaxena19@gmail.com

[b] Faculty of Chemistry, University of Warsaw, Pasteura 1, 02-093 Warsaw, Poland

[c] Center for Superfunctional Materials, Department of Chemistry, Ulsan National Institute of Science and Technology (UNIST), 50 UNIST-gil, Ulsan, 44919, South Korea

[d] Laboratory of Organic Electronics Department of Science and Technology, Linköping University, Norrköping, SE-60174, Sweden

2 Materials & methods

2.1 Experiment

A known amount of fine powdered biowaste (*Saccharum offici-narum*) was soaked in $Fe(NO_3)_3 \cdot 9H_2O$ aq. solution with different concentration of Fe^{3+} for 24 h in 1:4 (g mL^{-1}). Three samples were prepared by choosing 1, 2 and 8% (wt%) of Fe^{3+} concentration (w.r.t. bio-waste weight). The prepared samples were dried at 60 °C (12 h) followed by carbonization at 900 °C (temperature required for graphitization in presence of transition metal) under controlled heating (10 °C min^{-1}) under N_2 flow (20 mL min^{-1}) at 1 atm pressure. After an hour, the furnace was allowed to cool to RT under N_2 flow. The control sample CFe-0 was synthesized without Fe^{3+}-precursor under identical reaction condition. The iron-treated samples were referred as CFe-1, CFe-2, and CFe-3, which represents the 1, 2 and 8% (wt%, wrt initial bio-waste weight) of iron content respectively.

2.2 Characterization

Material characterization. The Brunauer–Emmett–Teller (BET) surface area analyzer was used to record nitrogen sorption isotherms at 77 K (Belsorp Max, Japan). Pore size distribution plots were taken from the desorption isotherms using the Barrett–Joyner–Halenda (BJH) model. The samples were degassed for 12 hours at 200 °C under vacuum before to measurement. Powder X-ray diffraction (PXRD) with Cu–K$_\alpha$ radiation was recorded across a range of 5–80° with a scan speed of 3° min^{-1} (Rigaku X-ray diffraction ultima-IV, Japan). Thermo Scientific™ Talos™ F200S High-Resolution Transmission Electron Microscope was used to examine the surface morphology of the samples (HRTEM). The PHI 5000 Versa ProbII, FEI Inc., was used to perform X-ray photoelectron spectroscopic (XPS) characterization. Raman spectra was recorded using Horiba Jobin Yvon Xplora Plus V1.2 Multiline with 532 nm excitation wavelength. Electrochemical characterization was performed using OrigaLys ElectroChem multichannel workstation equipped with Autolab RRDE setup. Inductively coupled plasma – optical emission spectrometry (ICP-OES) analysis has been performed using Optima 5300 DV, PerkinElmer, USA.

Electrochemical measurements. Electrocatalytic ink was prepared by mixing of active material and vulcan carbon (1:1 w/w) in the solvent mixture of water and isopropanol (200 µl each). Next, 6 µl of Nafion (5 wt% in IPA) was added to the mixture followed by sonication for 30 minutes to get fine dispersion. Now, 4 µl of freshly prepared electrocatalytic ink was drop casted over the GC electrode (working electrode, diameter 3 mm) and allowed to dry for 30 min at ambient condition. This GC electrode coated with electrocatalyst was used for electrochemical studies.

The ORR experiment was performed in a three-electrode system using rotating ring disc electrode (RRDE) in an aqueous solution of 0.1 M KOH. Glassy carbon (GC) electrode was used as working electrode, whereas platinum (Pt) electrode and Hg/HgO electrodes were served as counter and reference electrode, respectively. All potentials were converted with respect to reversible hydrogen electrode (RHE). All the electrochemical experiments were performed at the scan rate of 5 mV s^{-1}. Cyclic voltammetry (CV) experiments were done at static conditions whereas, linear sweep voltammetry (LSV) was performed at different rotation speeds in continuous flow of O_2. The EIS measurements were carried out at potential of −0.5 V *vs.* RHE under continuous O_2 flow over the electrolyte at and rotating speed of 1600 rpm. The EIS spectra were recorded in the frequency range of 0.1 to 10^5 Hz with an amplitude of 5 mV. The long-term stability for ORR catalysis was evaluated by chronoamperometry, performed in 0.1 M KOH solution at a static potential of 0.25 V. To avoid accumulation of gas bubbles on the electrode surface, the electrode was maintained at a fixed rotation during the experiment. The number of electrons were calculated using K–L plot. Rotating ring disk electrode (RRDE) voltammetry was used to calculate the number of electrons and the amount of H_2O_2 formed during ORR is based on the ratio of the disk and the ring current.

2.3 Number of electrons calculation

From K–L plot. The number of electrons involved in the reduction process was calculated using the Koutecký–Levich (K–L) equation:[19]

$$\frac{1}{j} = \frac{1}{j_L} + \frac{1}{j_K} = \frac{1}{B\omega^{1/2}} + \frac{1}{j_K}$$

$$B = 0.62nFC_0(D_0)^{2/3}\nu^{-1/6}$$

$$j_K = nFkC_0$$

where, j is the measured current density, j_K and j_K are the kinetic and diffusion-limited current densities, ω is the angular frequency of the RDE in radians per second, n is the number of electrons involved in the reaction, F is the Faraday constant (96 485 C mol^{-1}), D_0 is the diffusion coefficient of O_2 in the electrolyte (1.93 × 10^{-5} cm^2 s^{-1}), ν is the kinetic viscosity of the electrolyte (1.01 × 10^{-2} cm^2 s^{-1}), C_0 is the concentration of O_2 in the electrolyte (1.26 × 10^{-3} mol l^{-1}) and k is electron transfer rate constant.

RRDE. Rotating ring disk electrode (RRDE) voltammetry was used to calculate the number of electrons and the amount of H_2O_2 formed during ORR based on the ratio of the disk and the ring current as shown in the equations given below. For the RRDE experiments, the ring electrode was held at a potential of 1.5 V (*vs.* RHE) to oxidize H_2O_2.

$$n_e = \frac{4I_D}{I_D + \frac{I_R}{N}}$$

$$\% \ H_2O_2 = \frac{\frac{I_R}{N}}{I_D + \frac{I_R}{N}} \times 200$$

where, $N = 0.2678$ is the collection efficiency, I_D is the faradaic disk current, and I_R is the faradaic ring current.

DFT calculations. The Vienna *ab initio* simulation package (VASP) was used for all spin-polarized density functional theory (DFT) calculations.[20,21] The revised Perdew–Burke–Ernzerhof (RPBE) functional was employed to model the electronic exchange and correlations, while the Tkatchenko–Scheffler (TS) method was used to consider the dispersion correction with specified parameters.[22,23] The projector-augmented wave (PAW) method was employed to describe the electron–ion interactions.[24] A plane-wave basis set with a kinetic energy cutoff of 500 eV was applied to expand the wavefunctions. The Brillouin zone was sampled using the Monkhorst–pack $5 \times 5 \times 1$ k-point mesh. To prevent the interactions and influential force of periodic boundary, a large enough vacuum of 20 Å in the z-direction was set for all calculations. The electronic and geometry optimization of the structures were continued until both the energy difference and residual force between two consecutive iterations on each atom were below 10^{-5} eV and 0.01 eV Å^{-1}, respectively. The computational hydrogen electrode (CHE) method, under standard conditions as developed by Nørskov, was used to calculate the Gibbs free energy change (ΔG) of the reaction intermediates. The ΔG was calculated using $\Delta G = \Delta E + \Delta ZPE - T\Delta S$, where ΔE, ΔZPE, and ΔS represent the reaction energy of intermediates, change in zero-point energy, and entropy, respectively. The thermodynamic corrections caused by the solvent effect on adsorbent and adsorbate were investigated using VASPsol,[25] with a water medium represented by a dielectric constant of 80.

3 Results and discussion

3.1 Morphology characterization

FESEM analysis was carried out to study the surface morphology of the composites. FESEM of CFe-0 shows irregular sheet morphology (Fig. 1a and b). The FESEM image of iron doped composites, CFe-1, CFe-2, and CFe-3 are shown in Fig. 1c–h. The

high magnification FESEM images of CFe-1, CFe-2, and CFe-3 confirm sheet type morphology with embedded nanoparticles. To confirm the elemental distribution, elemental mapping has been performed for CFe-1, CFe-2 and CFe-3 and shown in respective columns (Fig. 1i–k). The FESEM image taken during elemental mapping suggested the particles are distributed on the surface. The Fe density in the elemental mapping has gradually increased from CFe-1 to CFe-3 as Fe percentage increases in the composite. The O element concentration has also increased as suggested by elemental mapping from CFe-1, CFe-2, and CFe-3. The particles shown in the SEM image (first column) are clearly visible in Fe and O mapping confirms them as iron oxides nanoparticles which are in corroboration with PXRD analysis, discussed later. Further, the electrochemical performance of these synthesized composite materials has been analysed in alkaline medium (0.1 M KOH).

The surface area and the pore size distribution of materials had characterized using N_2 adsorption–desorption at 77 K to know the surface area and pore size. The adsorption–desorption curves of CF-2 were ascribed to typical type IV profile (Fig. S1e†). The surface area of CFe-2 is $\sim$930 m^2 g^{-1} which is $\sim$25% higher compared to that of CFe-0 ($\sim$740 m^2 g^{-1}). The pore size distribution (PSD) for CFe-2 revealed pore diameters in the range of 0.4–1.7 nm (Fig. S1f†). The porous structure is advantageous because of its large surface area and easy accessibility of surface-active sites. The N_2 adsorption–desorption, pore-size distribution plots and textural properties for CFe-0, CFe-1, CFe-2 and CFe-3 are tabulated (Table 1 and Fig. S1†). It is noteworthy here that, electrochemical property of any material is also dependent upon the electrochemically active surface area (ECSA) rather than only physical surface area which is explained further.

Further, PXRD analysis was performed to determine crystallographic structure. CFe-0 shows broad peaks for (002) and (100) for amorphous carbon (Fig. 2a). The sharp peaks in PXRD of CFe-1, CFe-2 and CFe-3 confirm the crystalline nature of the samples (Fig. 2b–d). The sharp peaks in PXRD are marked for the corresponding planes of carbon and Fe$_3$O$_4$. For instance, CFe-2 PXRD shows the sharp peaks at $2\theta = 25.6°$, $44.6°$, and $57.2°$ corresponding to the (002), (101), and (004) planes of graphite (Fig. 2c).[26] The lattice spacing calculated for the (002) plane is 3.5 Å which is very close to the lattice spacing observed by HRTEM (3.7 Å). The peaks at $2\theta = 37.6°$ and $43.1°$ corresponds to the (112) and (121) plane of Fe$_3$C (ref. code 01-085-0871). The peaks at $2\theta = 30.2°$, $35.6°$, $45.7°$, $53.6°$, $62.7°$ corresponds to the (022), (131), (242), and (044) crystal planes of Fe$_3$O$_4$ (ref. code 96-900-5839). The presence of graphitic structure, Fe$_3$O$_4$, and Fe$_3$C as a hybrid structure is also supported
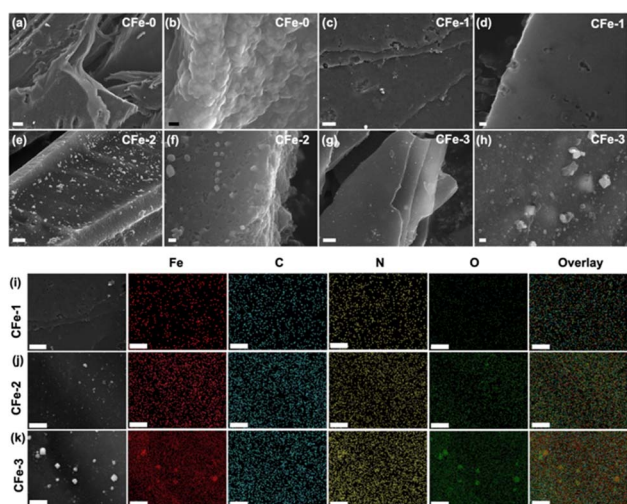
Fig. 1 FESEM image of (a and b) CFe-0; (c and d) CFe-1; (e and f) CFe-2; (g and h) CFe-3. Elemental mapping of (i) CFe-1, (j) CFe-2, (k) CFe-3 samples (scale bar (a, c, e and g) 1 μm; (b, d, f and h) 100 nm; (i–k) 2 μm).

Table 1 Textural properties of CFe-0, CFe-1, CFe-2, and CFe-3

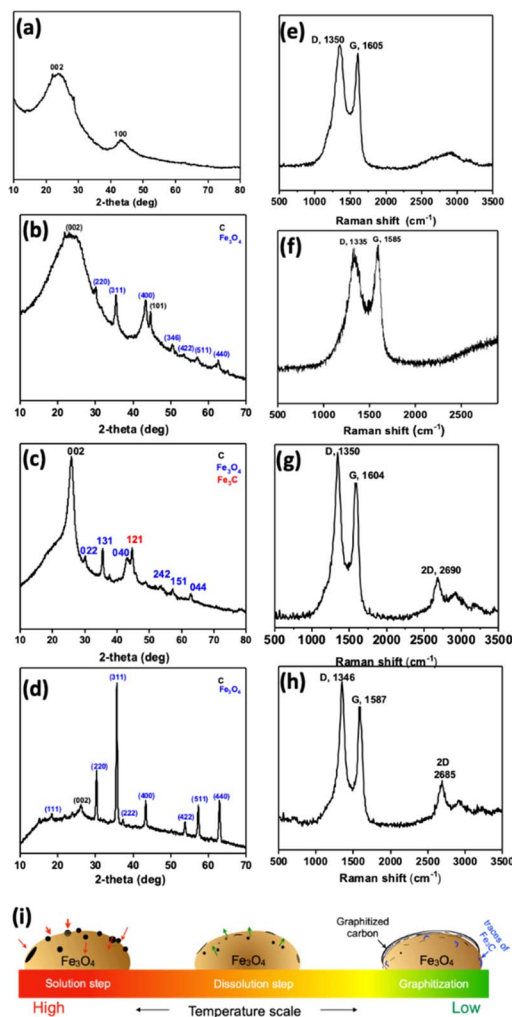| Textural properties	CFe-0	CFe-1	CFe-2	CFe-3
Surface area (m^2 g^{-1})	740	623	930	462
Total pore volume (cm^3 g^{-1})	0.33	0.32	0.53	0.50

Fig. 2 PXRD and Raman of (a and e) CFe-0, (b and f) CFe-1, (c and g) CFe-2 and (d and h) CFe-3, (i) graphitization scheme.

through HRTEM analysis. Fe_3C synthesis and graphitization process in CFe-2 is fascinating and explained further.

Further Raman spectroscopy was performed to investigate the carbon structure. Raman spectra of all the samples show D and G band corresponding to disorder and sp^2 hybridized carbon (Fig. 2e–h). The D- and G-bands are positioned at an average value of 1343 and 1590 cm^{-1}, respectively. The presence of graphitized structure is confirmed by the appearance of a new band at 2685 cm^{-1} corresponds to the 2D band that appears in CFe-1, CFe-2, and CFe-3. The D- and G-bands are well separated as Fe-content is increased from CFe-1 to CFe-3, suggesting increase in graphitized nature of the sample. Fe is a well-known catalyst for multi-walled carbon nanotubes, graphene growth at 900 °C or higher temperature.[27–30] The growth mechanism of MWCNT and graphene could be explained based upon the "solution-dissolution" mechanism based on the temperature-dependent carbon diffusion in iron (Fig. 2i). A considerable number of O atoms lead to the nucleation of Fe^{3+} ions and further formation of Fe_3O_4 particles at a higher temperature. At a high temperature, the carbon diffuses into the Fe_3O_4 particles

and, upon cooling, carbon precipitates out as a disordered graphitized structure due to its catalytic activity and temperature-dependent solubility. The presence of graphitized carbon is noteworthy that might be expected to enhance the stability of the ORR catalysts.[31] The traces of iron carbide are also formed due to the soluble carbon, which couldn't precipitate out upon cooling.

X-ray photoelectron spectroscopy (XPS) was employed to investigate the surface chemical composition of CFe-2. The survey spectrum clearly shows the presence of Fe, C, and O in synthesized material (Fig. 3a). The intensity of the Fe 2p peak is rather low compared to the peak intensity of C 1s ascribed to the minimal amount of Fe_3O_4 nanoparticle decoration on carbon support. The high-resolution Fe 2p spectrum of CFe-2 shows two broad peaks at 710.6 and 725.5 eV which are separated by split spin–orbit components of 14.9 eV (Fig. 3). The spectrum is deconvoluted into six peaks. It is well known that an increased valence state leads to an increment in the binding energy of the element. The intense peaks at 710.6 eV and 723.8 eV correspond to bivalent iron (Fe^{2+}) of $2p_{3/2}$ and $2p_{1/2}$, respectively while peaks at 712.8 and 725.8 eV are ascribed to trivalent iron (Fe^{3+}) of $2p_{3/2}$ and $2p_{1/2}$. The remaining two peaks are located at 718.1 and 725.6 could be attributed to satellite peaks. The high-resolution C 1s and O 1s spectra are shown in Fig. 3c and d. The high intense peak at 284.5 eV corresponds to graphitic carbon and the small peak at 286.3 eV corresponds to singly bonded C–O (Fig. 3c). The O 1s spectral band is further deconvoluted into three peaks at a binding energy of 530.8 eV, 532.1 eV, and 533.4 eV as shown in Fig. 3d. These peaks respectively correspond to surface-adsorbed H_2O, hydroxide (OH^-), and oxygen anion (O_2^-) in Fe_3O_4.

ORR electrocatalytic study. The ORR activity of synthesized composite materials (CFe-0, CFe-1, CFe-2, and CFe-3) are first evaluated by cyclic voltammetry (CV) and linear scan voltammetry (LSV) in O_2 saturated electrolyte solution. All the samples show reduction peak at 0.61 V suggesting that all the composite materials are electrochemically active toward ORR (Fig. 4a).
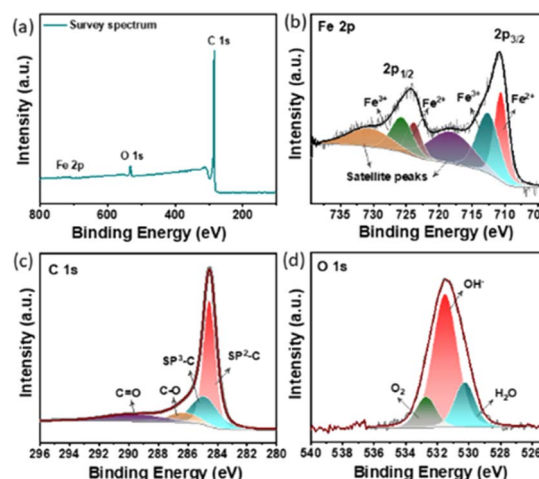

Fig. 3 XPS spectra of CFe-2 (a) survey spectrum (b) Fe 2p (c) C 1s and (d) O 1s.
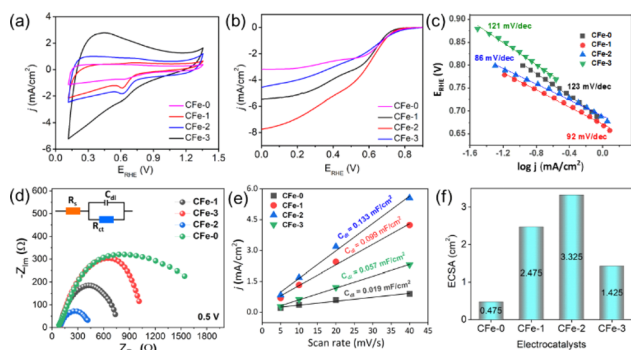
Fig. 4 (a) Cyclic voltammogram, (b) LSV at 1600 rpm, (c) Tafel slope, (d) EIS spectra (e) current densities ($\Delta J = J$ anode $- J$ cathode, at 0.453 V *vs.* RHE) *vs.* scan rate slope (e) and (f) ECSA bar graph for different electrocatalysts.

Further to confirm the ORR activity order of the synthesized composites, linear scan voltammetry (LSV) has been performed. CFe-2 shows the highest ORR activity supported by the current density at 1600 rpm (Fig. 4b). Superior ORR activity of CFe-2 was supported by comparative electrochemically active surface area (ECSA) and Tafel slope. Comparatively, CFe-2 shows highest current density of -7.7 mA cm^{-2} as compared with the CFe-0 (-3.2 mA cm^{-2}), CFe-1 (-5.5 mA cm^{-2}) and CFe-3 (-4.5 mA cm^{-2}) at 1600 rpm. To study the O$_2$ reduction kinetics, Tafel slope was plotted (Fig. 4c). Impressively, the slope of CFe-2 is 86 mV dec^{-1}, which is lower than CFe-0 (123 mV dec^{-1}), CFe-1 (92 mV dec^{-1}) and CFe-3 (121 mV dec^{-1}). This illustrates that the CFe-2 composite could enhance the process of mass transport indicating a favourable kinetic activity which is essential for ORR. Thus CFe-2 has been chosen for further detailed structural and electrochemical analysis. In order to understand comparative excellent ORR performance of CFe-2, the EIS and electrochemically active surface area (ECSA) were performed.[32] The EIS was performed to investigate the interfacial charge transfer phenomenon at the electrode/electrolyte interface. The EIS spectra for all the electrocatalyst are shown in Fig. 4d. All the electrocatalysts showed semicircular arc. The inset of Fig. 4d shows the fitted equivalent circuit. The measured charge transfer resistance (R_{ct}) values for CFe-0, CFe-1, CFe-2, and CFe-3 are 1448 Ω, 630 Ω, 307 Ω, and 912 Ω, respectively. The R_{ct} values follows the same trend as the ORR activity order of synthesized electrocatalysts. The lower R_{ct} value of CFe-2 indicates the better charge transfer property which leads to improved electrocatalytic activity. The ECSA is another important parameter which plays a crucial role towards the electrochemical performance. The ECSA of catalyst is calculated using formula ECSA = C_{dl}/C_s where C_{dl} and C_s signifies the double layer capacitance and capacitance of an atomically smooth planar surface of the catalyst per unit area under identical electrolyte conditions respectively.[33] The CV measurements were carried out at various scan rates (5 to 40 mV s^{-1}) in the region of 0.2–0.6 V (*vs.* RHE). A linear trend is observed (Fig. 4e) by plotting the difference in anodic and cathodic current densities at a potential of 0.453 V (*vs.* RHE). It is noteworthy that

CFe-2 catalyst endures larger C_{dl} (0.133 mF cm^{-2}) than that of CFe-1 (0.099 mF cm^{-2}), CFe-3 (0.057 mF cm^{-2}) and CFe-0 (0.019 mF cm^{-2}) suggesting that CFe-2 has more exposed active sites and thus showing exceptional electrochemical activity. Further the CFe-2 shows highest ECSA (3.325 cm^2) followed by CFe-1 (2.475 cm^2), CFe-3 (1.425 cm^2) and CFe-0 (0.475 cm^2), which supports the trend towards electrocatalytic activity towards oxygen reduction reaction (Fig. 4f). The ECSA order of electrocatalysts is corroborated with the BET surface area calculated using N$_2$ adsorption–desorption.

The CFe-2 cyclic voltammogram recorded in the O$_2$ saturated electrolyte shows a reduction peak at 0.61 V *vs.* RHE (Fig. 5a), which is absent in the N$_2$-atmosphere, unambiguously suggests CFe-2 potential to catalyse ORR. Further, LSV of CFe-2 was performed at 100–2500 rpm rotation speeds that didn't reach to limiting current with increasing rotation speed (Fig. 5b) and LSV of ring and disc current is given as Fig. 5c. This increasing trend in LSV suggests that the ORR process is still under mixed kinetics and diffusion despite the large overpotentials applied. It could be related to prepared carbon composite's intrinsic catalytic activity and porosity.[34] The maximum current density at the highest rotation speed might be due to the abundant O$_2$ dissolution and diffusion in the electrolyte by the continuous flow of O$_2$.[35]

Importantly, the onset potential (E_{onset}, the potential at which the current density reaches to -0.1 mA cm^{-2}) and half wave potential ($E_{1/2}$, the potential corresponding to half of the maximum current density value) to catalyze ORR is 0.82 V *vs.* RHE and 0.65 V *vs.* RHE respectively for the CFe-2 compared with the literature (Table S1†). The higher activity of CFe-2 is due to the synergistic effect of Fe$_3$O$_4$ and Fe$_3$C nanoparticles with carbon matrix, which is further proven by comparative LSV analysis of Fe$_3$O$_4$ and carbon layer separately. Note that the formation of Fe$_3$C was in a trace quantity, so its role in electrocatalytic behaviour is not very clear at the present stage. The maximum current density obtained for CFe-0 (only carbon) and Fe$_3$O$_4$ (Sigma Aldrich, India) are -3.2 mA cm^{-2} (Fig. 4b) and -1.8 mA cm^{-2} (Fig. S2†), respectively, which are less than that of CFe-2. The highest current density of CFe-2 compared to its
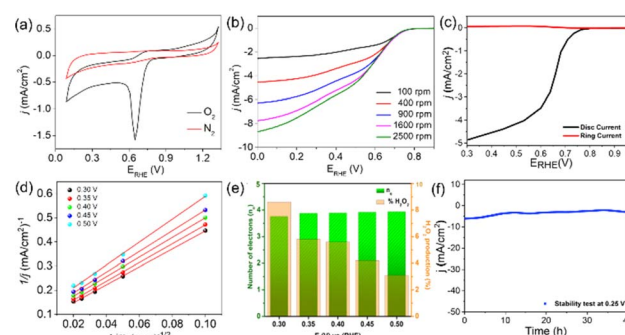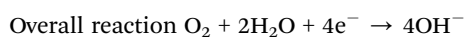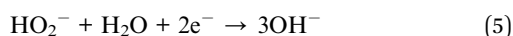

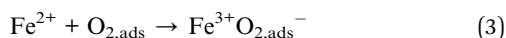**Fig. 5** CFe-2 (a) CV in N$_2$ and O$_2$-saturated 0.1 M KOH; scan rate: 5 mV s^{-1}, (b) LSV at different scan speeds, (c) LSV of ring and disc current (d) K–L plots, (e) number of electrons transferred and average peroxide production, (f) chronoamperometric response of CFe-2 at 0.25 V *vs.* RHE over 40 h.

single components confirms that the CFe-2 ORR performance is due to the synergistic effect of Fe_3O_4 and the carbon layer.

Further, the linearity of the K–L plot between j^{-1} and $\omega^{-1/2}$ indicates the first-order reaction kinetics (Fig. 5d). Typically, the benchmark electrocatalyst for ORR, such as Pt/C, utilized a direct $4e^-$ pathway which does not proceed *via* the formation of peroxide intermediate.[34] This has been further validated by the RRDE experiment. The number of electrons calculated between the potential range 0.3–0.5 V through the RRDE experiment was found to be 3.7–3.9 (Fig. 5e), which is in good agreement with K–L plot. The K–L and RRDE plots indicated that the ORR process catalyzed by CFe-2 is a close $4e^-$ process; therefore, water is the primary product in the ORR process. As estimated, H_2O_2 formed during ORR was found to be 3.1–8.6% in the potential range of 0.3–0.5 V (Fig. 5f). Mechanistically, the O_2 molecule in transition metal oxides gets adsorbed (eqn (2)), followed by a reduction step (eqn (3)). Then it forms HO_2^- (eqn (4)), which further reduces into OH^- (eqn (5)).[36,37] So the overall reaction follows $4 e^-$ pathways. The mechanism for ORR can be explained based on the following steps. Further, the catalytic stability test was performed up to 40 h at the static potential of 0.25 V *vs.* RHE at 1600 rpm (Fig. 5f). The CFe-2 demonstrates good catalytic stability even after 40 h during the ORR process.

$$Fe^{3+} + e^- \leftrightarrow Fe^{2+} \tag{1}$$

$$O_2 \rightarrow O_{2,ads} \tag{2}$$

$$Fe^{2+} + O_{2,ads} \rightarrow Fe^{3+}O_{2,ads}^- \tag{3}$$

$$O_{2,ads}^- + H_2O + e^- \rightarrow HO_2^- + OH^- \tag{4}$$

$$HO_2^- + H_2O + 2e^- \rightarrow 3OH^- \tag{5}$$

Overall reaction $O_2 + 2H_2O + 4e^- \rightarrow 4OH^-$

To gain a deeper understanding of the extraordinary catalytic performance of CFe-2, the active sites and four-electron pathway mechanism of ORR is studied through theoretical calculations based on density functional theory (DFT) (Fig. S3 and S4†). Herein, we investigated the mechanism for ORR under alkaline conditions, as shown in Fig. 6c. The calculated reaction free energy diagram at 0 V depicts that each electron transfer step maintains the downhill direction, indicating a spontaneous ORR reaction. The fourth elementary step, which involves the desorption of OH* is identified as the potential limiting step, corresponding to an overpotential of 0.39 V (Fig. 6a). The results demonstrate that ORR catalytic activity is limited due to the strong binding of OH on Fe center. As the oxygen adsorption on the surface is significantly influenced by the electronic structure and density of states of the catalyst, we calculated the projected density of states (PDOS), for O-adsorbed CFe-2 (Fig. 6b). The presence of occupied d-electrons near the Fermi level facilitates the transfer of charge from partially filled d-orbitals to the π_{2p*} orbital of O atom. To determine the charge transfer between the active Fe site and adsorbed O atom, Bader charge and charge density difference (CDD) analysis are carried out (Fig. 6d). It is observed that the active Fe site loses approximately $0.96|e|$, while the adsorbed
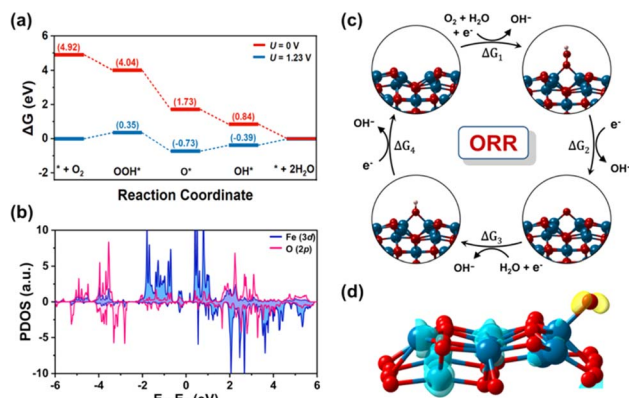

Fig. 6 (a) ORR free energy diagram at potential of 0 V and 1.23 V. (b) Calculated PDOS for O-adsorbed CFe-2 substrate, Fermi level is set to zero. (c) Schematic mechanistic pathway for ORR (d) charge density difference, the charge accumulation and depletion are in yellow and cyan colors, respectively.

oxygen gains approximately $0.79|e|$. Consistent with Bader charge analysis, the CDD also indicates that electrons are transferred from Fe to the O atom (ESI†).

As CFe-2 shows the best activity, we have performed the detailed surface morphology characterization of CFe-2 using low and high-magnification TEM (Fig. 7a–e). Fig. 7a suggests that Fe_3O_4 nanoparticles (high contrast) are embedded homogeneously in the thin layer carbon matrix. The dense contrast area is Fe_3O_4, whereas yellow arrows indicate the graphitized carbon layers in the CFe-2 (Fig. 7b). The yellow and red colored dotted area in Fig. 7b is magnified further in Fig. 6c and d, respectively. The two different types of lattice-spacing, 2.39 Å and 3.7 Å could be seen at the near edge and edges of CFe-2 (Fig. 7c). The lattice spacing of 2.39 Å corresponds to the (121) plane of Fe_3C (ref code 96-901-6232). The graphitic layers can be easily seen at the top-right corner adjacent to Fe_3C (Fig. 7c). The 3.7 Å lattice spacing corresponds to the (002) graphite plane, further corroborated by PXRD and Raman. The lattice spacing is slightly higher than the standard 3.4 Å, suggesting the
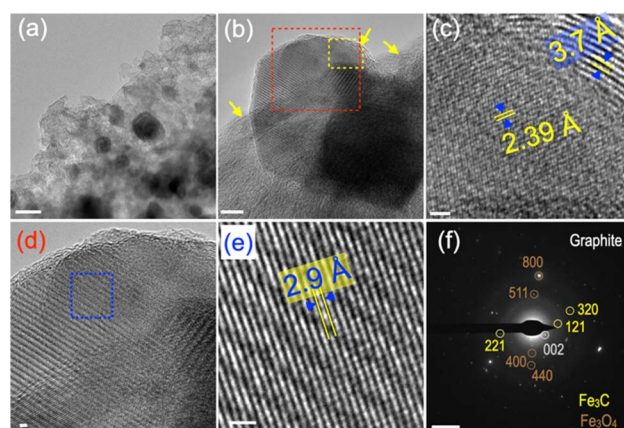

Fig. 7 HRTEM images of (a–e) CFe-2. (h) SAED pattern of CFe-2. Scale bar: (a) 50 nm (b) 10 nm (c–e) 1 nm (f) 5 nm^{-1}.

formation of disordered graphitic layers in CFe-2. Fe_3C and graphitic layer together confirm the "solution-dissolution" growth mechanism and are schematically represented in Fig. 7c. The blue color marked area in Fig. 7d is further magnified in Fig. 7e, where lattice fringes could be visible, suggesting the high crystallinity of the particle. The lattice spacing of 2.9 Å corresponds to the (022) plane of Fe_3O_4 (ref. code 96-900-5839). The SAED pattern of CFe-2 exhibits characteristic diffraction spots for different planes of Fe_3O_4, Fe_3C, and graphitized carbon (Fig. 7f). Energy-dispersive X-ray spectroscopy (EDS) analysis was performed to quantify the C, N, O, and Fe content in CFe-2. (Fig. S5 and Table S2†). The iron content in CFe-2 is 1.3% (at%), which agrees with XPS data. However, EDS is a short-range analysis, while XPS is surface-sensitive. To quantify the total iron content in CFe-2, ICP-OES analysis has been performed as per standard protocol. The total iron content in CFe-2 is 8.41 at%. Element analysis has been performed to quantify the carbon, nitrogen, and hydrogen in CFe-0, CFe-1, CFe-2, and CFe-3 samples (Table S2†).

4 Conclusions

In brief, we have synthesized an iron oxide–carbon composite using agri-waste as a carbon precursor. Moreover, no activation step is involved in the composite synthesis process, which helps reduce synthesis costs. Electrochemically active surface area (ECSA = 3.325 cm^2), double layer capacitance (C_{dl} = 0.133 mF cm^{-2}), and Tafel slope (86 mV dec^{-1}) reveal the good ORR activity of the catalyst. The near to 4 electron transfer process and H_2O as primary product suggests that the synthesized electrocatalyst will impact efficient electrocatalyst designing for ORR in alkaline solution.

Author contributions

M. S. conceived the idea. S. R. M., P.·B. J. performed experiments, characterizations, analysis, writing manuscript. R. A., G. L. has performed the theoretical calculations. AKS, Z. K. assisted in microscopic and electrochemical data analysis.

Conflicts of interest

There are no conflicts to declare.

Acknowledgements

Notes and references

1 M. M. Fernández, E. M. Periñán, S. Royuela, J. Martínez, F. Zamora, L. Encarnacion and J. Segura, *Appl. Mater. Today*, 2022, **26**, 101384.

2 M. Al-Dhaifallah, M. A. Abdelkareem, H. Rezk, H. Alhumade, A. M. Nassef and A. G. Olabi, *Int. J. Energy Res.*, 2021, **45**, 1587–1598.

3 Q. Ma, H. Jin, J. Zhu, Z. Li, H. Xu, B. Liu, Z. Zhang, J. Ma and S. Mu, *Adv. Sci.*, 2021, **8**, 2102209.

4 J. Ren, Z. Shi and Y. Huang, *Int. J. Hydrogen Energy*, 2023, **48**, 12333–12341.

5 Z. Ahmed and V. Bagchi, *New J. Chem.*, 2021, **45**, 22012–22033.

6 B. Chang, S. Wu, Y. Wang, T. Sun and Z. Cheng, *Nanoscale Horiz.*, 2022, **7**, 1340–1387.

7 X. Huang, C. Wang and Y. Hou, *Chem. Commun.*, 2022, **58**, 8884–8899.

8 S. Nagappan, M. Duraivel, S. A. Hira, K. Prabakar, C.-S. Ha, S. H. Joo, K. M. Nam and K. H. Park, *J. Mater. Chem. A*, 2022, **10**, 987–1021.

9 J. Ma, W. Zhang, F. Yang, Y. Zhang, X. Xu, G. Liu, H. Xu, G. Liu, Z. Wang and S. Pei, *RSC Adv.*, 2024, **14**, 4607–4613.

10 Z. Zhang, S. Yang, H. Li, Y. Zan, X. Li, Y. Zhu, M. Dou and F. Wang, *Adv. Mater.*, 2019, **31**, 1805718.

11 J. Woo, J. S. Lim, J. H. Kim and S. H. Joo, *Chem. Commun.*, 2021, **57**, 7350–7361.

12 W. Gu, L. Hu, J. Li and E. Wang, *Electroanalysis*, 2018, **30**, 1217–1228.

13 S. Pérez-Rodríguez, D. Sebastián, C. Alegre, T. Tsoncheva, N. Petrov, D. Paneva and M. J. Lázaro, *Electrochim. Acta*, 2021, **387**, 138490.

14 J. Barrio, A. Pedersen, S. Favero, H. Luo, M. Wang, S. C. Sarma, J. Feng, L. T. T. Ngoc, S. Kellner, A. Y. Li, A. B. J. Sobrido and M.-M. Titirici, *Chem. Rev.*, 2023, **123**, 2311–2348.

15 W. Zhong, Z. Xiao, Y. Luo, D. Zhang, X. Chen and J. Bai, *RSC Adv.*, 2023, **13**, 36424–36429.

16 M. S. Ahmed, H. Begum and Y.-B. Kim, *J. Power Sources*, 2020, **451**, 227733.

17 S. R. Manippady, A. Singh, C. S. Rout, A. K. Samal and M. Saxena, *ChemElectroChem*, 2020, **7**, 1928–1934.

18 S. Haghdan, S. Renneckar and G. D. Smith, in *Lignin in Polymer Composites*, ed. O. Faruk and M. Sain, William Andrew Publishing, 2016, pp. 1–11, DOI: 10.1016/B978-0-323-35565-0.00001-1.

19 H.-m. Kim, B.-c. Cha and D.-w. Kim, *RSC Adv.*, 2023, **13**, 26918–26924.

20 G. Kresse and J. Furthmüller, *Comput. Mater. Sci.*, 1996, **6**, 15–50.

21 R. Li, L. Zhang, Y. Wang, J. Bai, X. Li and C. Zhang, *RSC Adv.*, 2023, **13**, 27705–27713.

22 B. Hammer, L. B. Hansen and J. K. Nørskov, *Phys. Rev. B: Condens. Matter Mater. Phys.*, 1999, **59**, 7413–7421.

23 A. Tkatchenko and M. Scheffler, *Phys. Rev. Lett.*, 2009, **102**, 073005.

24 P. E. Blöchl, *Phys. Rev. B: Condens. Matter Mater. Phys.*, 1994, **50**, 17953–17979.

25 K. Mathew, R. Sundararaman, K. Letchworth-Weaver, T. A. Arias and R. G. Hennig, *J. Chem. Phys.*, 2014, **140**, 084106.

26 Z. Q. Li, C. J. Lu, Z. P. Xia, Y. Zhou and Z. Luo, *Carbon*, 2007, **45**, 1686–1695.

27 Y. J. Jung, B. Wei, R. Vajtai, P. M. Ajayan, Y. Homma, K. Prabhakaran and T. Ogino, *Nano Lett.*, 2003, **3**, 561–564.

28 C. Mattevi, C. T. Wirth, S. Hofmann, R. Blume, M. Cantoro, C. Ducati, C. Cepek, A. Knop-Gericke, S. Milne and C. Castellarin-Cudia, *J. Phys. Chem. C*, 2008, **112**, 12207–12213.

29 S. T. Neeli and H. Ramsurn, *Carbon*, 2018, **134**, 480–490.

30 I. Kholmanov, E. Cavaliere, C. Cepek and L. Gavioli, *Carbon*, 2010, **48**, 1619–1625.

31 H. Meng, Y. Liu, H. Liu, S. Pei, X. Yuan, H. Li and Y. Zhang, *ACS Appl. Mater. Interfaces*, 2020, **12**, 41580–41589.

32 G. Cheng, T. Kou, J. Zhang, C. Si, H. Gao and Z. Zhang, *Nano Energy*, 2017, **38**, 155–166.

33 J. Mohanta, B. Dey and S. Dey, *J. Chem. Eng. Data*, 2020, **65**, 2819–2829.

34 Z. Khan, S. O. Park, J. Yang, S. Park, R. Shanker, H.-K. Song, Y. Kim, S. K. Kwak and H. Ko, *J. Mater. Chem. A*, 2018, **6**, 24459–24467.

35 G. Zhong, S. Xu, L. Liu, C. Z. Zheng, J. Dou, F. Wang, X. Fu, W. Liao and H. Wang, *ChemElectroChem*, 2020, **7**, 1107–1114.

36 X. Ge, A. Sumboja, D. Wuu, T. An, B. Li, F. T. Goh, T. A. Hor, Y. Zong and Z. Liu, *ACS Catal.*, 2015, **5**, 4643–4667.

37 N. Parveen, Z. Khan, S. A. Ansari, S. Park, S. Senthilkumar, Y. Kim, H. Ko and M. H. Cho, *Chem. Eng. J.*, 2019, **360**, 415–422.